



High catalytic activity of magnetic FeO_x/NiO_y/SBA-15: The role of Ni in the bimetallic oxides at the nanometer level



Xingfa Li^{a,b}, Wanpeng Liu^a, Jianqing Ma^c, Yuezhong Wen^{a,c,*}, Zucheng Wu^b

^a Institute of Environmental Science, College of Environmental and Resource Sciences, Zhejiang University, Hangzhou 310058, China

^b Department of Environmental Engineering, State Key Laboratory of Clean Energy Utilization, Zhejiang University, Hang Zhou 310027, China

^c Zhejiang Provincial Key Laboratory of Organic Pollution Process and Control, Zhejiang University, Hangzhou 310058, China

ARTICLE INFO

Article history:

Received 5 December 2014

Received in revised form 29 April 2015

Accepted 15 May 2015

Available online 19 May 2015

Keywords:

Bimetallic catalyst

Fenton-like

Nanoparticles

Magnetic

Synergistic effect

ABSTRACT

Recently, great efforts have been devoted for improving the catalytic activity of the iron-based bimetallic oxide catalysts by taking advantage of the synergistic effects between Fe and the second metal. Herein, we report the preparation of a highly active and magnetic nickel–iron Fenton-like catalyst by fabricating uniform and highly dispersed mixed phase FeO_x/NiO_y in mesoporous material SBA-15 (Santa Barbara Amorphous-15). This bimetallic oxide catalyst achieved 99.3% removal of the dye Acid Red 73 in 1 h, while monometallic loaded catalysts reached 29.2% and 21.9% only. Besides, 65.81% TOC removal of Acid Red 73 (initial concentration of H₂O₂ was 4.0 mM) and more than 95% utilization efficiency of H₂O₂ were obtained by FeO_x/NiO_y/SBA-15 in 1 h, which were much higher than the traditional Fe²⁺ catalyst (only 49.81% and 28.56%, respectively). At last, this catalyst showed good reusability and can be easily separated by using a magnet. Characterization results confirmed that iron species including Fe₃O₄ and Fe₂O₃, nickel species including Ni(0) and NiO coexisted in the synthesized FeO_x/NiO_y/SBA-15. The test results and mechanism analysis showed that nickel species have positive contributions to the high catalytic activity of this catalyst.

© 2015 Elsevier B.V. All rights reserved.

1. Introduction

Nowadays, in catalysis fields, through the fabrication of multi-components and multi-interfaces catalysts, high catalytic activity and multi-function have been attained [1–4]. Particularly, catalysts with novel structural and/or electronic properties were achieved by incorporating the active compositions into porous materials with confined space, because small-sized nanoparticles with high catalytic activity will be obtained due to the confinement effect and size effect [4–9]. Additionally, local density of active sites would increase in narrow space [10,11]. Last but not the least, strong interaction between the surface of the porous material and active composition hinders the shedding of the nanoparticles [12]. Attracted by these favorable properties, heterogeneous Fenton-like catalysts based on porous materials as supports have been intensively investigated for wastewater treatment [6,13–18].

Among the kinds of porous materials, mesoporous SBA-15 (Santa Barbara Amorphous-15) has become a hotspot in the field of catalyst synthesis due to its large surface area, ordered channels or

poles, narrow pore size distribution and high structural stability in water [6,12,15,19–23]. More importantly, SBA-15 provides a suitable range of pore size (5–8 nm or more) for growth of nanoparticles in the confinement microenvironment [6,21,24]. On one side the pore size in the material should not be too small to load metal active composition, because the load capacity is limited and the blockages of the nanochannels may occur. On the other side if the pore size is too large (>50 nm, such as macroporous material), it is difficult to limit the size of nanoparticles in few nanometers. It has been reported that nanoparticles located inside the channels of SBA-15 have much higher catalytic activity than that outside the channels [21]. Therefore, great efforts have been devoted for encapsulating iron-based active composition into SBA-15 channels to improve the catalytic activity of the Fenton-like catalyst [6,15,21,23]. At the same time, there has been a strong interest in preparation of bimetallic (oxides) catalysts in Fenton-like degradation by taking advantage of the synergistic effect between two metal (oxides) [6,25,26]. However, what happens when several active compositions are immobilized together into the channels have rarely been reported.

In this paper, a catalyst that incorporated nickel–iron bimetallic oxides in SBA-15 were elaborately designed in order to obtain high-dispersity and small size. The exact roles of the second metal (here

* Corresponding author. Tel.: +86 571 88982421; fax: +86 571 88982421.
E-mail address: wenyuezhong@zju.edu.cn (Y. Wen).

refers to nickel) and the synergistic effects between iron and the second metal oxides in the catalytic process were carefully investigated. This catalyst was used to catalyze degradation of the dye Acid Red 73, a common type of anionic dye used in the textile, printing and dyeing industry [27–29]. Various characterization techniques were used to obtain the physical structure and chemical composition of the catalyst. Results showed, owing to the synergistic effects in the surface chemistry and in Fenton-like degradation at the nanometer level, the catalyst achieved excellent performance for dye removal with high mineralization degree and high utilization efficiency of H_2O_2 .

2. Materials and methods

2.1. Materials

Mesoporous silica SBA-15 ($\text{SiO}_2/\text{Al}_2\text{O}_3 \geq 500$; pore diameter: 6–8 nm; BET: $400\text{--}600\text{ m}^2\text{ g}^{-1}$) was purchased from Nanjing XFNano Material Tech Co., Ltd., China. $\text{Fe}(\text{NO}_3)_3 \cdot 9\text{H}_2\text{O}$ (AR), $\text{NiCl}_2 \cdot 6\text{H}_2\text{O}$ (AR) and hydrogen peroxide (GR, 30 wt%) were obtained from National Medicines Corporation Ltd. of China. Acid Red 73 (100%, molecular formula $\text{C}_{22}\text{H}_{14}\text{N}_4\text{Na}_2\text{O}_7\text{S}_2$, molecular weight 556.48, color index number 27290, structure is shown in Fig. S1 in Supporting information) was purchased from Gracia Chemical Technology Co., Ltd., China. Doubly distilled water was used throughout this study.

2.2. Preparation of the catalyst

The catalyst was prepared by incipient wetness impregnation and H_2 reduction, which is similar to the method that described in our previous work [6]. Before using it as a support, SBA-15 was dried at 80°C in a vacuum oven. 4 mL of acidified NiCl_2 solution with 53.198 g/L $\text{NiCl}_2 \cdot 6\text{H}_2\text{O}$ as nickel precursor was added into 1 g SBA-15 progressively and mixed by vigorous agitation. The mixture was shelved for 24 h and then dried in an oven at 85°C overnight. The precipitate was dehydrated at 105°C for 3 h and calcined at 400°C in air for 3 h. The calcined solid was impregnated with 4 mL of acidified $\text{Fe}(\text{NO}_3)_3$ solution containing 90.421 g/L $\text{Fe}(\text{NO}_3)_3 \cdot 9\text{H}_2\text{O}$ followed with drying and annealing through the same procedure as was performed for Ni. Finally, the solid was reduced by H_2 (20 mL/min) at certain temperature for 2 h. The optimal catalyst obtained was denoted as $\text{FeO}_x/\text{NiO}_y/\text{SBA-15}$ (calcined at 400°C in air and reduced by H_2 at 300°C). Correspondingly, the monometallic $\text{FeO}_x/\text{SBA-15}$ and $\text{NiO}_y/\text{SBA-15}$ catalysts were also prepared with corresponding mole of Fe or equal mole of Ni in $\text{FeO}_x/\text{NiO}_y/\text{SBA-15}$. For comparative purposes, a series of iron and nickel oxides-loaded SBA-15 samples were prepared under different preparation conditions including the total metal content in the catalyst, proportion to Ni and Fe and reduction temperature. The molar ratio of Ni and Fe was 1:1 in the $\text{FeO}_x/\text{NiO}_y/\text{SBA-15}$.

2.3. Characterization of the catalyst

N_2 adsorption–desorption isotherm was determined by TRIS-TAR II 3020 instrument (Micromeritics Instrument Corporation, USA), and pore size distribution was obtained from desorption branch of the isotherms by the BJH (Barret–Joyner–Hallender) method. In order to obtain an entirely direct view of the nanoparticles in the superpage of SBA-15, catalysts were embedded in Spurr's resin and cut into 60–80 nm thin sections. The samples were observed on a JEM-1230 transmission electronic microscope (JEOL, Japan). The XPS spectra were performed on an ESCALAB 250 electron spectrometer (Thermo Electron Corporation, USA) with Al K α radiation (1486.6 eV). All binding energies were calibrated by using

the C 1s peaks at 284.6 eV as references. The XRD patterns were collected on a XRD-6000 diffractometer (Shimadzu, Japan) with a Cu K α ray source ($\lambda = 0.154\text{ nm}$) at 40 kV and 40 mA. XANES signals of the Fe K-edge and Ni K-edge were measured using a transmission mode at beamline 14W1 of the Shanghai Synchrotron Radiation Facility (SSRF). The spectra were normalized to get information about the energy position of the edge. The freeware IFEFFIT was used to perform normalization and linear combination fitting in the same way for all spectra.

2.4. Performance tests of the catalyst

Fenton catalytic performance of the catalyst was tested in 100 mL flask, which was agitated at 160 rpm in a thermostatic shaker maintained at 25°C . The reaction mixture was initiated with 50 mL of AR73 at 50 mg/L and 0.6 g/L of catalyst at the desired pH. In addition to the dye and catalyst, a certain amount of H_2O_2 (30 wt%) was added. Dye concentration was monitored by sampling at regular time intervals and analyzed by using a Shimadzu UV-2401PC UV–vis spectrometer (Kyoto, Japan) at 509 nm. Total organic carbon (TOC) values of dyes after reaction were determined by a Shimadzu spectrometer (TOC-VCPh) with a non-dispersive infrared detector. Concentration of H_2O_2 in the solution was measured by spectrophotometric determination using titanium sulfate at 400 nm.

3. Results and discussion

3.1. Catalytic reactivity of $\text{FeO}_x/\text{NiO}_y/\text{SBA-15}$ for Fenton-like reaction

In a preliminary study, a batch of experiments was executed under a given condition (pH 3, catalyst dosage = 0.6 g/L, temperature = 25°C , initial concentration of AR 73 = 50 mg/L and H_2O_2 dosage = 10 mM) to evaluate the catalytic activities of the samples. It can be seen from Fig. 1, low oxidation degradation of the dye AR 73 was obtained with H_2O_2 alone. But when bimetallic oxides were supported in SBA-15, $\text{FeO}_x/\text{NiO}_y/\text{SBA-15}$ achieved high removal rate (reaches up to 97.6% in 30 min and 99.3% in 1 h). In order to verify the presence of Fenton-like catalytic degradation, the adsorption effect of $\text{FeO}_x/\text{NiO}_y/\text{SBA-15}$ was also investigated. It can be seen that the gap of the dye AR 73 removal between adsorption (no H_2O_2) and Fenton reaction increased from 18.3% in 5 min to 68.0% in 1 h, indicating that degradation reaction actually happened. In the meantime, the extent of mineralization is one of the most important factors to evaluate a new oxidative degradation system. Besides, the value of TOC indicates loss of aromaticity and overall degree of compound degradation. As shown in Fig. 1, it can be seen that the TOC residue was about 40% when dyes were treated with $\text{FeO}_x/\text{NiO}_y/\text{SBA-15}$ for 1 h. The results indicated that dye AR 73 was almost completely destroyed and a considerable amount was mineralized. In order to survey the active species in the dye degradation, the probe compounds isopropanol and ethanol were used (50 mM) in this study because they are selective for $\cdot\text{OH}$ [30,31], and the latter can react with possibly produced ferryl ion in Fenton reaction [30]. As shown in Fig. 1, degradation of the dye AR 73 was considerably inhibited by the addition of isopropanol and ethanol, which validates the contribution of strongly oxidizing radicals to dye degradation.

It is obviously that this bimetallic catalyst achieved high catalytic activity for AR 73 removal, but the respective contributions of two metals in the catalytic process are still not clear. It can be seen from Fig. 2, when monometallic loaded catalysts $\text{FeO}_x/\text{SBA-15(i)}$ and $\text{NiO}_y/\text{SBA-15(i)}$ were used, which contained same amount of metal loading to the corresponding metal in the $\text{FeO}_x/\text{NiO}_y/\text{SBA-15}$,

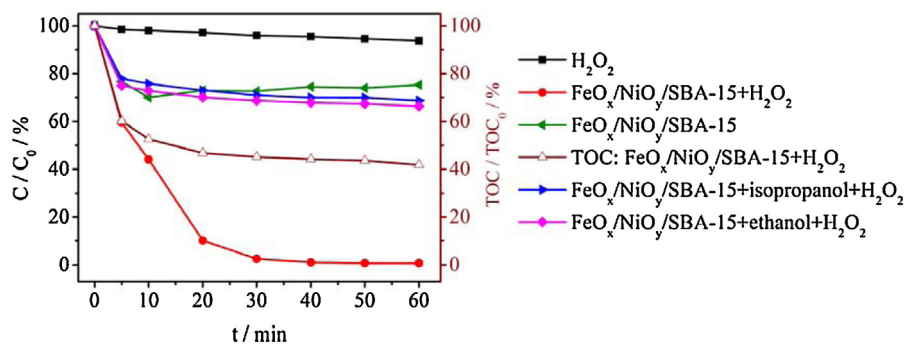


Fig. 1. Fenton-like degradation of AR 73 by $\text{FeO}_x/\text{NiO}_y/\text{SBA-15}$ (AR 73 50 mg/L, 50 mL, pH 3, catalyst 0.6 g/L, H_2O_2 10 mM).

they all had poor AR 73 removal efficiency in 1 h (29.2% and 21.9%, respectively). Of course, it can be easily calculated that even equal amounts of $\text{FeO}_x/\text{SBA-15}$ (i) and $\text{NiO}_y/\text{SBA-15}$ (i) were physically mixed, the removal rate of the joint was also far less than that of $\text{FeO}_x/\text{NiO}_y/\text{SBA-15}$ under same conditions although they have same metal species and same total metal loadings. More interestingly, when Fe content was increased in Fe loaded catalyst ($\text{FeO}_x/\text{SBA-15}$ (ii)) as high as the total metal loadings in $\text{FeO}_x/\text{NiO}_y/\text{SBA-15}$, it exhibited low AR 73 removal rate (about 52% in 1 h). Similar situation happened in $\text{NiO}_y/\text{SBA-15}$ (ii), which has same Ni amount to total metal loadings in $\text{FeO}_x/\text{NiO}_y/\text{SBA-15}$. In addition, it can be found that Fe loaded catalyst is more efficient than Ni loaded catalyst in the AR 73 removal ($\text{FeO}_x/\text{SBA-15}$ (i) > $\text{NiO}_y/\text{SBA-15}$ (i), $\text{FeO}_x/\text{SBA-15}$ (ii) > $\text{NiO}_y/\text{SBA-15}$ (ii)) although they have same moles of metals. The molar ratio of Ni:Fe was 1:1 in the $\text{FeO}_x/\text{NiO}_y/\text{SBA-15}$ (see experimental section), $\text{FeO}_x/\text{SBA-15}$ (ii) actually had twofold Fe loading to $\text{FeO}_x/\text{NiO}_y/\text{SBA-15}$, the latter still achieved the greatest catalytic activity, implying that synergistic effect between Fe and Ni exists in AR 73 removal.

3.2. Physical structure of $\text{FeO}_x/\text{NiO}_y/\text{SBA-15}$

In order to understand the performance-structure relationship, physical structure of $\text{FeO}_x/\text{NiO}_y/\text{SBA-15}$ were comprehensively investigated. If the active components were successfully confined in the pores of SBA-15, BET surface area and pore volume would decrease after the metals impregnation due to the part blockage of the pore system [5,32,33]. It can be observed from the N_2 adsorption-desorption isotherms in Fig. S2 in Supporting information and pore size distribution curves shown in Fig. S3 in Supporting information, all samples supported by SBA-

Table 1

Structure parameters of all SBA-15 supported samples.

Samples	Surface area (m ² /g)	Pore volume (cm ³ /g)	Pore diameter (nm)
Pure SBA-15	558	0.94	5.75
$\text{FeO}_x/\text{SBA-15}$	411	0.62	5.14
$\text{NiO}_y/\text{SBA-15}$	414	0.61	5.21
$\text{FeO}_x/\text{NiO}_y/\text{SBA-15}$	374	0.55	5.11

15 in this study (pure SBA-15, $\text{FeO}_x/\text{SBA-15}$, $\text{NiO}_y/\text{SBA-15}$ and $\text{FeO}_x/\text{NiO}_y/\text{SBA-15}$) showed a typical IV isotherm with H1 hysteresis loop at the relative pressure $p/p_0 = 0.6-0.7$, indicating that they still keep a well-defined hexagonal pore structure same as the pure SBA-15. But when metals were introduced, BET surface areas and pore volumes decreased greatly comparing with that of pure SBA-15 (shown in Table 1), suggesting successful incorporation of metal species inside SBA-15 channels, and this is highly consistent with the XRD results (shown in Fig. S4 in Supporting information).

In order to get an entirely direct view of the nanoparticles in the supracage of SBA-15, TEM images of the slice were investigated. From the Fig. 3, it can be seen that all the samples loaded on SBA-15 retained the hexagonal porous silica structure. Obviously, introducing metal species in the channels did not affect the framework of the mesoporous materials. Fig. 3b shows that iron oxide in $\text{FeO}_x/\text{SBA-15}$ mainly developed in the forms of dark and rod-like nanowires inside the pores of SBA-15. In contrast, Ni nanoparticles in $\text{NiO}_y/\text{SBA-15}$ are highly dispersed with an average size of about 20 nm (Fig. 3c). The diameter of Ni species is much larger than that the pore diameter of $\text{NiO}_y/\text{SBA-15}$, suggesting that the silica walls are pushed away when nickel oxide parti-

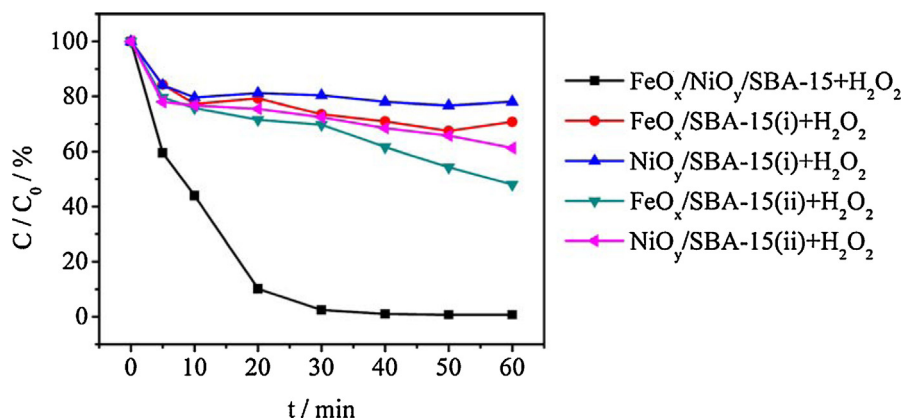


Fig. 2. Comparisons of Fenton-like degradation of AR 73 by bimetallic catalyst and corresponding monometallic catalysts (AR 73 50 mg/L, 50 mL, pH 3, catalyst 0.6 g/L, (i) the catalyst containing same amount of metal loading to the corresponding metal in the $\text{FeO}_x/\text{NiO}_y/\text{SBA-15}$; (ii) the catalyst containing as high metal content as the total metal loadings in $\text{FeO}_x/\text{NiO}_y/\text{SBA-15}$; H_2O_2 10 mM).

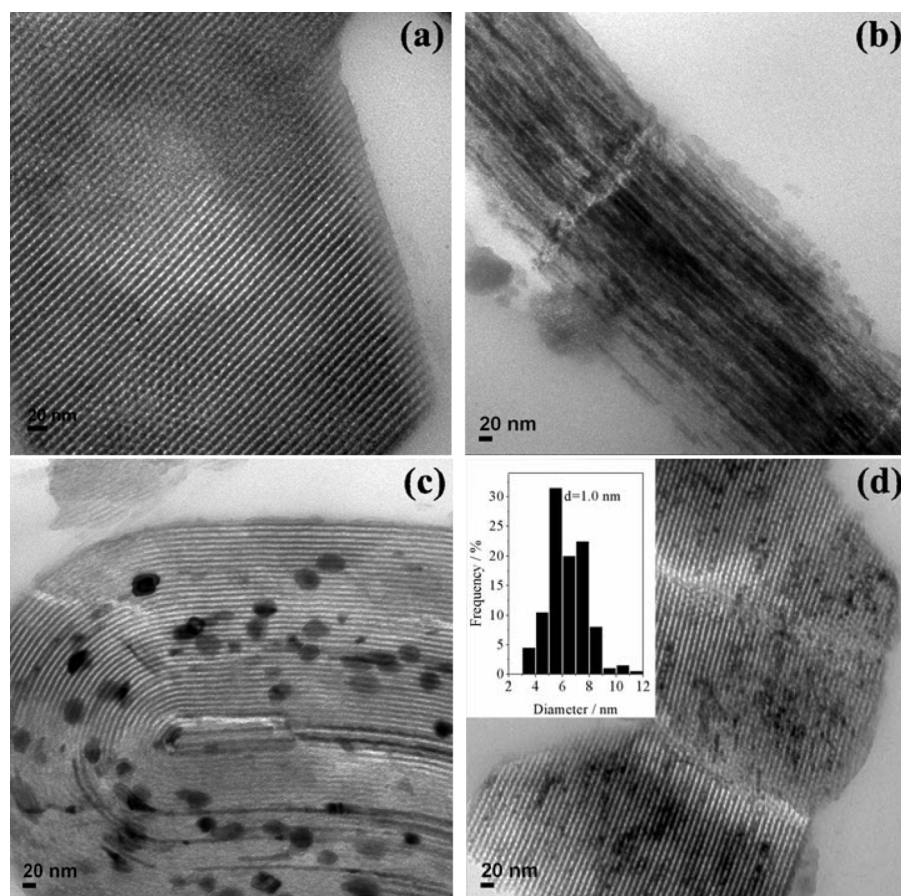


Fig. 3. TEM images of the following samples: (a) pure SBA-15, (b) $\text{FeO}_x/\text{SBA-15}$, (c) $\text{NiO}_y/\text{SBA-15}$ and (d) $\text{FeO}_x/\text{NiO}_y/\text{SBA-15}$.

cles crystallize [21]. Interestingly, from Fig. 3d, it can be seen that nanoparticles in $\text{FeO}_x/\text{NiO}_y/\text{SBA-15}$ have a better uniform and narrow distribution centered at 5.0–8.0 nm and the size of particles is significantly smaller than that in $\text{FeO}_x/\text{SBA-15}$ and $\text{NiO}_y/\text{SBA-15}$. Furthermore, it was found that Fe species displayed in the forms of nanowires with tens nm of length when they were incorporated alone in the pores of SBA-15, but nanowires disappeared in the Ni and Fe two-component catalyst. That is, there were no obvious separate nanoclusters of Fe species and Ni species in the channels. This phenomenon may be ascribed to the effect of deposition of oxide nanoparticles on the surface of a second (host) oxide. EDX elemental mapping of Ni and Fe has been carried out to justify this point. It can be seen from Fig. 4, both Ni and Fe can be clearly identified on the surface of $\text{FeO}_x/\text{NiO}_y/\text{SBA-15}$. And they all have uniform distributions, corresponding to the small size and well dispersed nanoparticles when iron was incorporated on the surface of nickel oxides. The cause may be explained as below. On the one side, during the impregnation of Ni in preparation of $\text{FeO}_x/\text{NiO}_y/\text{SBA-15}$, the Ni^{2+} ions are homogeneously distributed throughout the pores of SBA-15 and growing up with high dispersion. Followed by the impregnation of Fe, part of Ni oxides (host) partially dissolved and acted as seeds for the growth of iron oxide nanoparticles, which resulted in the production of small sized nanoparticles in $\text{FeO}_x/\text{NiO}_y/\text{SBA-15}$. On the other side, strong metal-support interaction was present between nickel species (host) and surface of SBA-15, the nickel species were stabilized via the 1:1 nickel phyllosilicate phase [12] and spherical or ellipsoidal of nickel nanoparticles were formed. Owing to the highly dispersed nanoparticles with small size, much higher reaction activity of $\text{FeO}_x/\text{NiO}_y/\text{SBA-15}$ was obtained [5].

3.3. Chemical composition of $\text{FeO}_x/\text{NiO}_y/\text{SBA-15}$

In order to explore the phases of active components in the catalyst, large-angle XRD patterns of $\text{FeO}_x/\text{NiO}_y/\text{SBA-15}$ and monometallic $\text{FeO}_x/\text{SBA-15}$ and $\text{NiO}_y/\text{SBA-15}$ catalysts were investigated. It can be found from Fig. 5 that different from $\text{FeO}_x/\text{SBA-15}$ and $\text{NiO}_y/\text{SBA-15}$, intensities of peaks in the $\text{FeO}_x/\text{NiO}_y/\text{SBA-15}$ get broad and short, which can be explained by the presence of highly dispersed and small particles [8,17]. Furthermore, diffraction peaks at 33.1° , 49.4° , 54.0° , 62.4° and 63.9° , assigned to (1 0 4), (1 1 0), (0 2 4), (1 1 6), (2 1 4) and (3 0 0) typical characteristic peaks of $\alpha\text{-Fe}_2\text{O}_3$ (JCPDS card, File no. 89-0597). However, it is worth notice that the peaks at 35.6° and 62.4° were near or overlapped the peaks (*) of reference Fe_3O_4 (JCPDS card, File no. 88-0315), so the existence of Fe_3O_4 should not be ruled out. On the other hand, the peaks at 44.5° and 51.8° , assigned to (1 1 1) and (2 0 0) reflections of the cubic Ni lattice (JCPDS card, File no. 04-0850). Beside metallic Ni and $\alpha\text{-Fe}_2\text{O}_3$, peaks at 37.2° and 43.3° respond to (1 1 0) and (2 0 0) of NiO (JCPDS card, File no. 89-7131) were also observed, while no peaks such as Fe–Ni alloy were clearly observed. It can be explained by the close vicinity between metallic Ni and Fe in the channels of $\text{FeO}_x/\text{NiO}_y/\text{SBA-15}$, which causes a strong interaction between Fe species and Ni species, and does not lead to the formation of the Fe–Ni alloy. As we know, catalytic ability of active components depends on the oxidation states, and which can be identified by XPS. From the XPS spectra shown in Fig. 6A, the $\text{Fe } 2p_{3/2}$ binding energy of 711.1 eV, the corresponding $\text{Fe } 2p_{1/2}$ peak at 724.9 eV and the corresponding satellite peak near 718 eV can be solely attributed to the presence of Fe^{3+} ions in $\alpha\text{-Fe}_2\text{O}_3$ [34,35]. Meanwhile, main photopeaks at 856.4, 874.2 eV and broad satellite peak near 863 eV

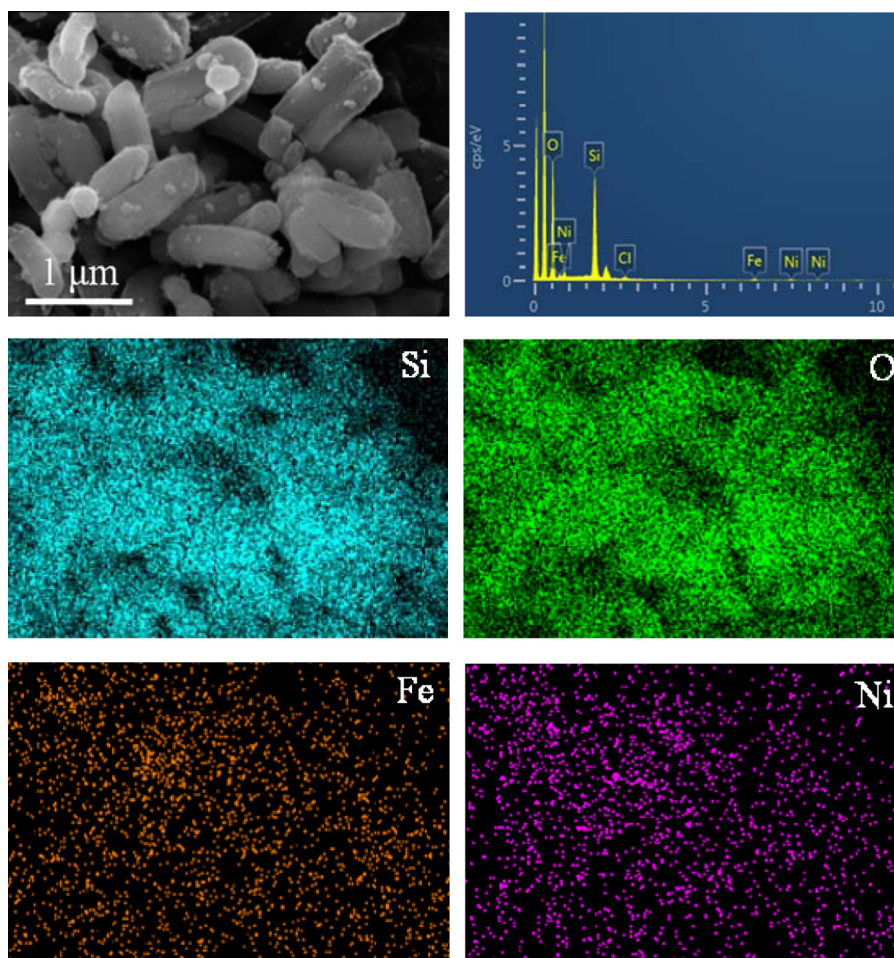


Fig. 4. SEM photograph and elemental mapping images of $\text{FeO}_x/\text{NiO}_y/\text{SBA-15}$, Si, O, Fe and Ni with color superposition.

in Fig. 6B, neither belong to metallic Ni nor NiO, because the binding energy of Ni $2p_{3/2}$ (856.4 eV) in $\text{FeO}_x/\text{NiO}_y/\text{SBA-15}$ is higher than the characteristic of Ni^{2+} in NiO (854.6–854.9 eV) [12,36], indicating the strong interaction between nickel-support on the surface of the catalyst [12].

The local structural environment of metal in catalyst also has an effect on the catalytic activity, and which can be characterized by XANES. In XANES analysis, it has been established that a linear

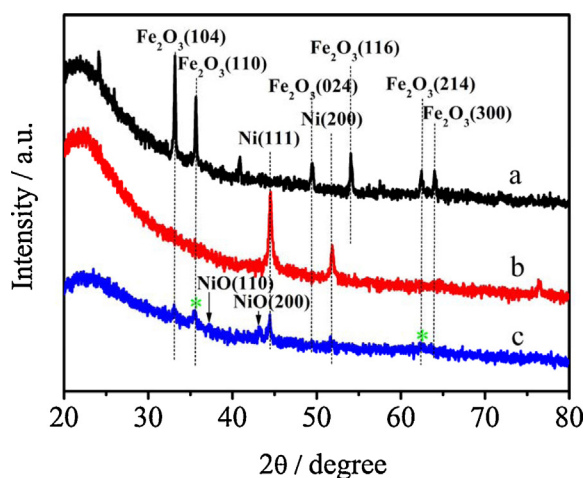


Fig. 5. Large-angle XRD patterns of (a) $\text{FeO}_x/\text{SBA-15}$, (b) $\text{NiO}_y/\text{SBA-15}$ and (c) $\text{FeO}_x/\text{NiO}_y/\text{SBA-15}$.

relationship exists between the shift of the edge and the valence state, because same type of neighbor atoms in nearest coordination shells have similar symmetries and arranges [37]. Therefore, by comparing the adsorption edge profiles and pre-edge peaks between the sample and reference compounds, the local structural environment and valence state of an atom in a sample can be determined. The XANES spectra of the catalysts, along with the reference materials, were displayed in Fig. 7. In Fig. 7A, it can be seen that the XANES spectra of Fe K-edge in $\text{FeO}_x/\text{NiO}_y/\text{SBA-15}$ nanoparticles is very similar to that of standard Fe_2O_3 spectrum. Besides, the energy position and intensity of the pre-edge peak of the catalyst is also in good agreement with the reference Fe_2O_3 , indicating that Fe atom in catalyst coordinates to O atom and Fe species in $\text{FeO}_x/\text{NiO}_y/\text{SBA-15}$ mainly exist in the form of Fe_2O_3 . However, it is noteworthy that the position of main maximum at 7132.7 eV in $\text{FeO}_x/\text{NiO}_y/\text{SBA-15}$ located between Fe_3O_4 and Fe_2O_3 , and the intensity was higher than the reference Fe_2O_3 . Furthermore, the shoulder peak at 7130 eV was disappeared comparing with Fe_2O_3 , implying that a small part of the Fe_3O_4 presents in the catalyst. Fig. 7B shows that the Ni K-edge in $\text{FeO}_x/\text{NiO}_y/\text{SBA-15}$ exhibits analogous profile with the standard spectra of nickel oxides, but does not exactly same with any one of them, implying that Ni atom in catalyst coordinates to O atom and multiple valence states of Ni coexist in $\text{FeO}_x/\text{NiO}_y/\text{SBA-15}$. To quantify the specific compositions of the catalysts, the spectra were fitted with a linear combination of the reference spectra. Quantitative results, along with the contributions of the different references, are displayed in Table 2. The data indicated that iron species including Fe_3O_4 and Fe_2O_3 and nickel

Table 2

Linear combination of XANES spectra of SBA-15 supported catalysts.

Reference catalyst	Fe			Ni	
	Fe ₃ O ₄	Fe ₂ O ₃	Ni	NiO	Ni ²⁺ in Ni-phyllsilicate [12]
FeO _x /SBA-15	7.7%	92.3%	/	/	/
NiO _y /SBA-15	/	/	3.8%	20.4%	75.8%
FeO _x /NiO _y /SBA-15	5.7%	94.3%	13.9%	43.7%	42.4%

species including Ni(0) and NiO coexisted in FeO_x/NiO_y/SBA-15, which was in line with the results of XRD and XPS.

3.4. Influences of Ni on the catalytic reactivity

Fig. 2 has indicated that the synergistic effect works in the Fenton-like reaction between Fe and Ni species. It is known that iron and iron oxides all can catalyze Fenton-like degradation, but whether nickel and nickel oxides are capable of redox cycling and produces •OH in Fenton-like reaction are not clear, and whether Ni species can indirectly promote the reaction rate and degradation efficiency are still unknown. According to one report [38], the presence of Ni facilitated the reduction of Fe³⁺–Fe²⁺ on the iron oxide surface, and bimetallic nickel–iron particles showed a higher reactivity than monometallic iron in the treatment of contaminants. But others demonstrated that Ni addition did not enhance hydroxyl radical formation [39], which is usually the objective of advanced

oxidation processes used to treat organic contaminants. Therefore, the exact role of Ni in the catalytic process still demands further investigation.

In order to examine the Fenton or Fenton-like catalytic behavior of nickel, Ni species (contain equal moles of Ni to FeO_x/NiO_y/SBA-15) including Ni²⁺, Ni(0) and NiO were tested in H₂O₂ added dye solution. It can be seen from Fig. S5 in Supporting information that there are no obvious degradation were observed by using Ni²⁺, Ni(0) and NiO as catalysts in 1 h, but when dosages of them were raised to 0.03 g (same weight as FeO_x/NiO_y/SBA-15) in 50 mL solution and reaction time was extended to 24 h (1440 min) (shown in Fig. S6 in Supporting information), slight Fenton or Fenton-like degradations was observed in 1 h and enhanced removal of the dye AR 73 was observed in 24 h. Therefore, it can be presumed that NiO and Ni²⁺ have mild Fenton-like catalytic activity and they are powerless in catalyzing Fenton-like reaction in short time.

In order to probe the influence of Ni content on catalytic activity of bimetallic oxides catalyst, monometallic loaded catalysts and

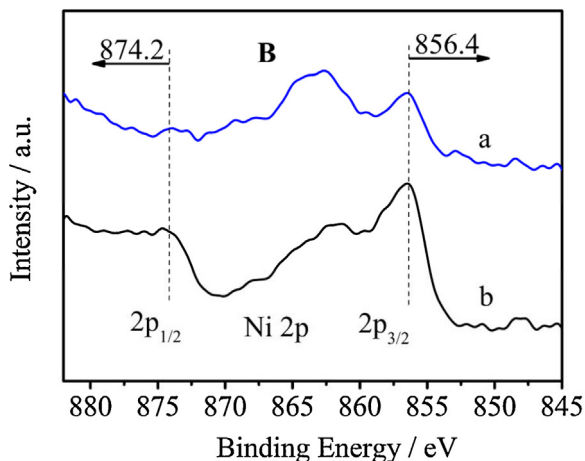
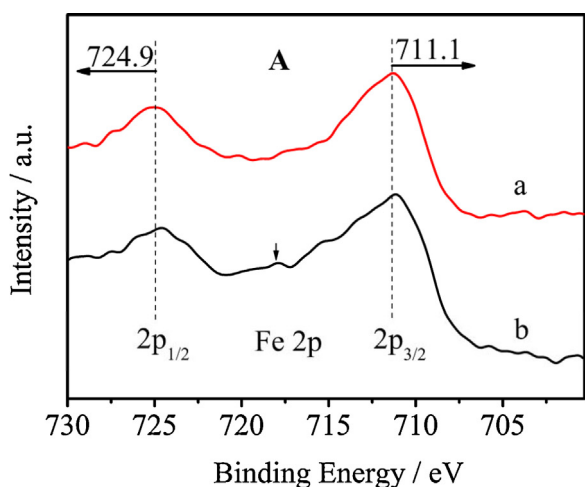


Fig. 6. (A) Fe 2p XPS spectra of (a) FeO_x/SBA-15 and (b) FeO_x/NiO_y/SBA-15, (B) Ni 2p XPS spectra of (a) NiO_y/SBA-15 and (b) FeO_x/NiO_y/SBA-15.

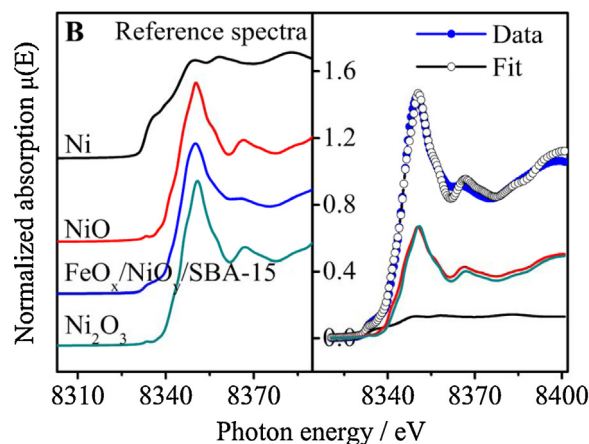
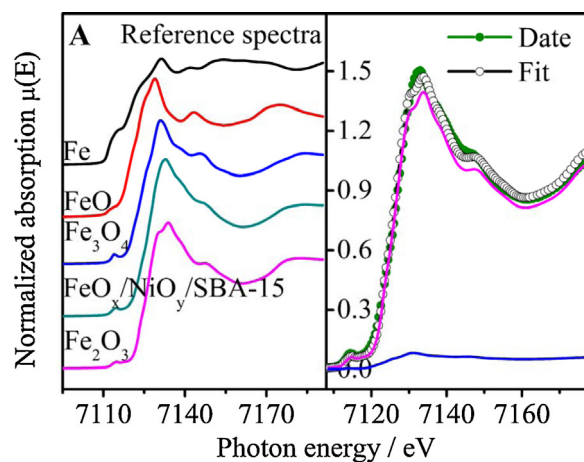


Fig. 7. (A) Fe K-edge XANES spectra and Fit curve of FeO_x/NiO_y/SBA-15, (B) Ni K-edge XANES spectra and Fit curve of FeO_x/NiO_y/SBA-15.

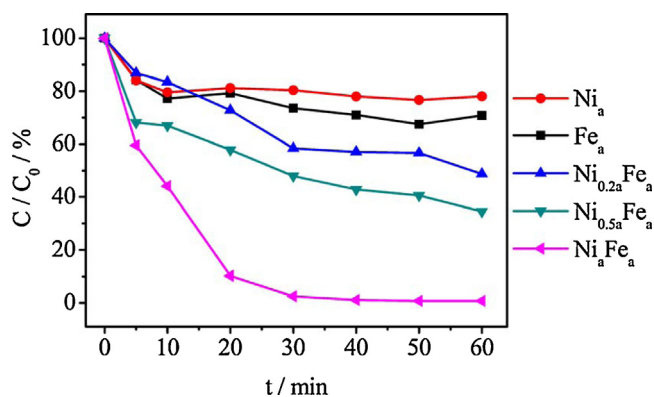


Fig. 8. Effect of nickel introduction on dye degradation (the subscript represents the loaded amount (in mole) of metals, $a = 8.953 \times 10^{-4}$. AR 73 50 mg/L, 50 mL, pH 3, catalyst 0.6 g/L, H_2O_2 10 mM).

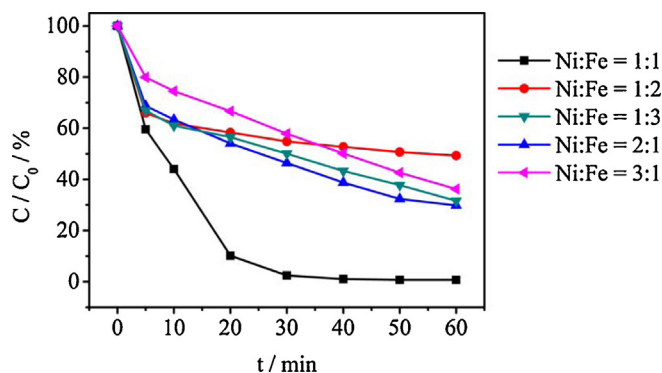


Fig. 9. Effect of proportion of loaded metals on dye degradation (AR 73 50 mg/L, 50 mL, pH 3, catalyst 0.6 g/L, H_2O_2 10 mM).

bimetallic composites with different Ni content were compared. It is obvious that (shown in Fig. 8) monometallic loaded catalysts (Ni_a and Fe_a , $a = 8.953 \times 10^{-4}$ mol) all have low dye removal, while when keeping the amount of iron unchanged, the removal rate greatly increased with increase of the nickel content. On the other side, the effect of proportion on catalytic activity was investigated when keeping the sum of two metals (in mole) Fe and Ni are same. Because when the proportion of Ni/Fe varied, they may form compounds with different atomic ratio, such as awaruite Ni_3Fe and spinel $NiFe_2O_4$, and the catalytic activity varied. Fig. 9 shows the removal rates by bimetallic Fe and Ni catalysts with same total amount of metals and different proportion, and it can be seen that the best removal rate was obtained when moles of Ni/Fe is 1:1.

3.5. Formation of FeO_x/NiO_y mixed-phase

In heterogeneous catalysis, the active chemical composition of a catalyst can work more efficiently only in particular composition and phase [2,3]. In this study, the catalyst was prepared under H_2 atmosphere, so the phase was controlled by reduction temperature (T_R) and the second element Ni. With the addition of Ni, new phases of nickel species, iron–nickel solid solution and alloy may be formed, and the phases will vary with the elevation of T_R . It can be seen from Fig. 10, almost same amount of the dye AR 73 removals were obtained by reduced catalyst at 200 °C and unreduced one. With increasing T_R from 300 °C to 500 °C, removal rates were much higher than that of unreduced one, but decreased successively, indicating that the catalysts may possess different valences and phases. The presumption can be easily confirmed by XANES analysis due to its high accuracy and resolution in valence characterization. Fig. 11 shows the XANES signals of the Fe K-edge and Ni K-edge of catalysts

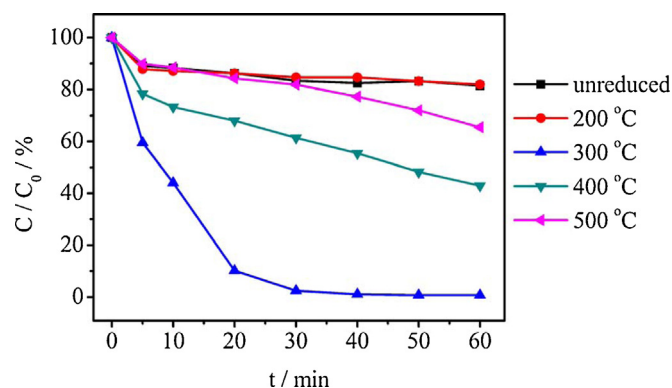


Fig. 10. Effect of reduction temperature on dye degradation (AR 73 50 mg/L, 50 mL, pH 3, catalyst 0.6 g/L, H_2O_2 10 mM).

Table 3

TOC removal and utilization efficiency of H_2O_2 (η).

Material	TOC removal (%)	η (%) ^a	η (%) ^b	Refs.
$FeO_x/NiO_y/SBA-15^c$	58.13	93.41	30.73	This study
$FeO_x/NiO_y/SBA-15^d$	65.81	>95	87.35	This study
Fe^{2+e}	49.81	28.56	27.30	This study
Fe–Cu oxides	39	42	28.5	[13]
$BiFeO_3$	90	64.4	6.57	[14]
Fe_3O_4	6	7.06	0.44	[14]
Fe_3O_4	51	73	31.2	[17]

^a Calculated by Luo's method.

^b Calculated by total amount of the H_2O_2 added.

^c Initial concentration of H_2O_2 is 10.0 mM.

^d Initial concentration of H_2O_2 is 4.0 mM.

^e $FeSO_4$ was used as the homogeneous Fenton catalyst, initial concentration of H_2O_2 is 10.0 mM.

with different T_R . It can be seen from Fig. 11A, no significant differences were noticed in absorption edges between the catalysts and standard Fe_2O_3 when T_R less than 300 °C. In parallel, similar phenomenon were observed between the catalysts and standard Ni_2O_3 shown in Fig. 11B. With the further increasing of T_R , the adsorption edges all shift to low energy, indicating that new crystal phases were formed as a function of the chemical composition of catalysts, and the average valence of the element was moving to low even zero valence. Obviously, 300 °C is a dividing line, that is, mixed phases of nickel were obtained at 300 °C by H_2 reduction. Ascribing to this mixed-phase of FeO_x/NiO_y , best performance of catalytic activity was achieved in Fig. 1.

3.6. Utilization efficiency of H_2O_2

In Fenton or Fenton-like degradation, dosage of H_2O_2 is a noteworthy factor because H_2O_2 is an expensive commodity, and it is dangerous to produce, and for transportation and storage [6]. Fig. 12 shows that when initial concentration of H_2O_2 increased, consumption rate of H_2O_2 decreased continuously, but TOC removal increased at first, and then gradually and slowly decreased, means that overdosed H_2O_2 doesn't lead to higher TOC removal. This is because H_2O_2 acts as a scavenger of the $\cdot OH$ at high H_2O_2 concentration [16]. Luo et al. had proposed that the utilization efficiency of H_2O_2 can be calculated by the ratio of H_2O_2 amount used for pollutant degradation against the total amount of the consumed H_2O_2 in the reaction [40]. According to this theory, TOC removal rate and utilization efficiency of H_2O_2 were calculated by Eq. (1) and listed in Table 3. It can be seen that TOC removal over $FeO_x/NiO_y/SBA-15$ was higher by 8.3% than that for Fe^{2+} at the same reaction condition, and utilization efficiency of H_2O_2 over $FeO_x/NiO_y/SBA-15$ was 3.3 times for Fe^{2+} . What is more, 65.81% of TOC removal was obtained by $FeO_x/NiO_y/SBA-15$ and almost all of the H_2O_2 in the system par-

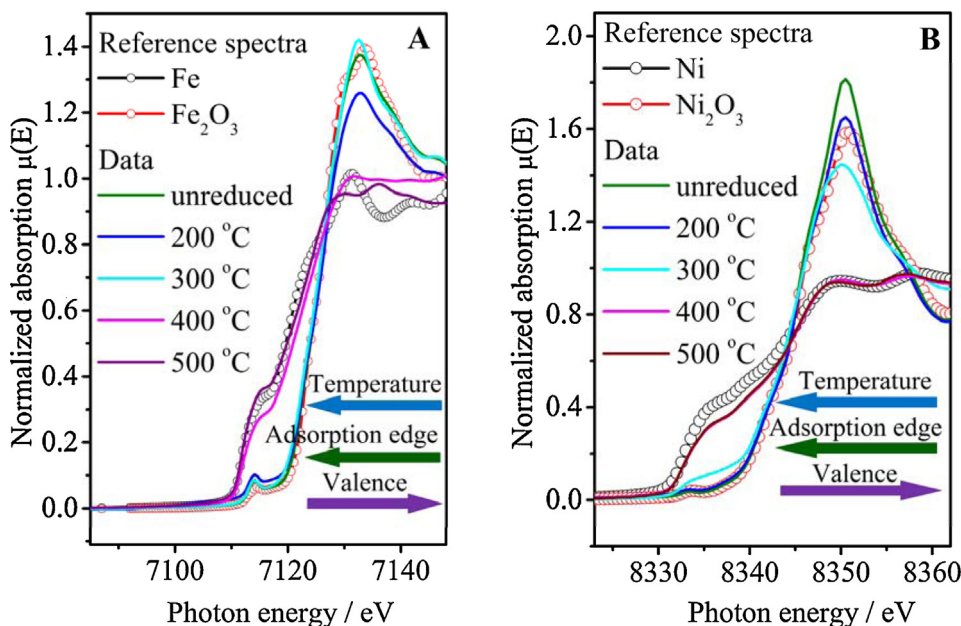
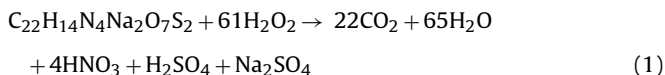


Fig. 11. (A) Fe K-edge XANES spectra and (B) Ni K-edge XANES spectra of catalysts prepared under different reduction temperature.

anticipated in mineralization of AR 73 when initial concentration of H_2O_2 was 4.0 mM. Thus demonstrating amazing ability of mineralization and high utilization efficiency of H_2O_2 , implying minimal waste by $\text{FeO}_x/\text{NiO}_y/\text{SBA-15}$ for decomposing H_2O_2 to H_2O and O_2 which has no contribution to TOC removal.

Although Luo's method reflects the mineralization ability of a catalyst, it does not consider the excess of H_2O_2 which leads to huge waste because it cannot be extracted and used in next time. Therefore, denominator in their calculation formula should be the total amount of the H_2O_2 added in the reaction system, rather than the amount of the consumed H_2O_2 in the reaction. Based on this idea, utilization efficiency of H_2O_2 was recalculated. Data listed in Table 3 also shows that $\text{FeO}_x/\text{NiO}_y/\text{SBA-15}$ has higher efficiency of utilization of H_2O_2 than Fe^{2+} and other studies. Besides the high catalytic activity of the catalyst, the pronounced efficiency may ascribe to the low reactivity of Ni species with H_2O_2 , which increases the lifetime of adsorbed H_2O_2 and facilitates H_2O_2 release and increases the production of oxidant by reaction of iron species [41].



3.7. Reusability and recyclability of the catalyst

From the view of actual application, reusability is one of the most important problems in heterogeneous Fenton-like degradation. As shown in Fig. 13, it can be observed that $\text{FeO}_x/\text{NiO}_y/\text{SBA-15}$ showed high catalytic activity after seven consecutive runs. This result demonstrated that encapsulating the active components into the channels of ordered mesoporous SBA-15 remarkably reduces the release of active components and extends the life of catalyst. Furthermore, it has been shown that small part of Fe_3O_4 and Ni(0) (Table 2) are present in $\text{FeO}_x/\text{NiO}_y/\text{SBA-15}$, so the catalyst should have a magnetic or ferromagnetic property, which is conducive for the separation of the catalyst. The magnetization curve of $\text{FeO}_x/\text{NiO}_y/\text{SBA-15}$ was shown in Fig. 14. The corresponding magnetic parameters including saturation magnetization (M_s), remnant magnetization (M_r) and coercivity (H_c) of the catalyst are 3.36 emu g^{-1} , 0.922 emu g^{-1} and 472.07 Oe , respectively, suggest-

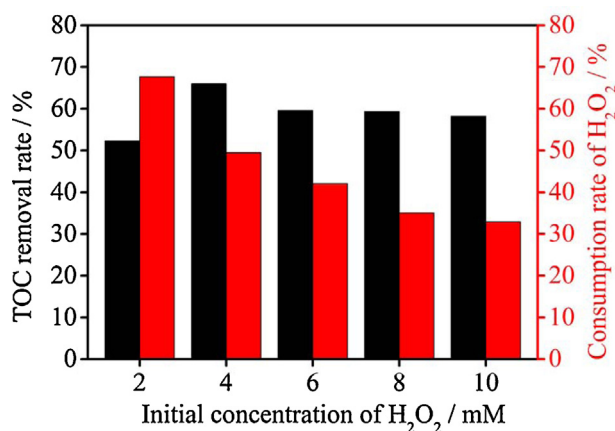


Fig. 12. Effect of H_2O_2 dosage on TOC removal and consumption rate of H_2O_2 (AR 73 50 mg/L, 50 mL, pH 3, catalyst 0.6 g/L).

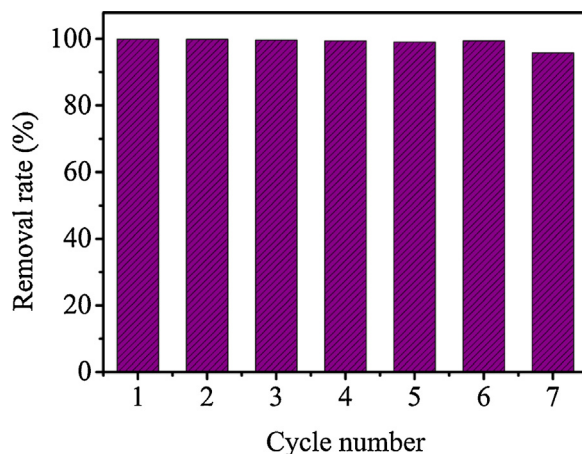


Fig. 13. Dye removal in different cycles (AR 73 50 mg/L, 50 mL, pH 3, catalyst 0.6 g/L, H_2O_2 10 mM).

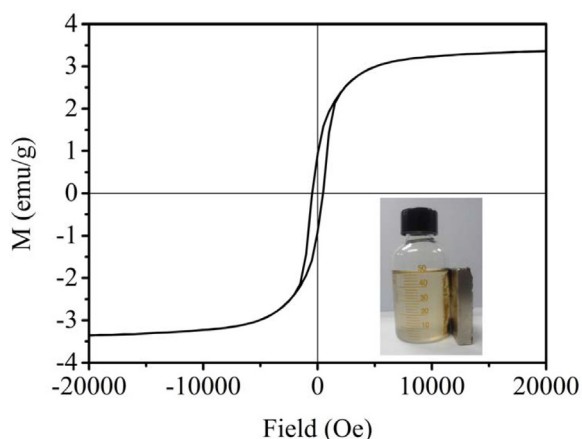


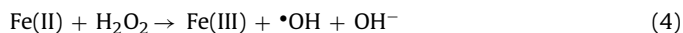
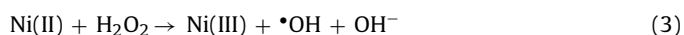
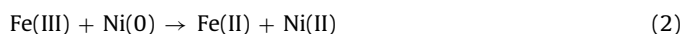
Fig. 14. Magnetization curve of $\text{FeO}_x/\text{NiO}_y/\text{SBA-15}$ and optical photo (inset) of the catalyst in the water solution separated by a magnet.

ing a significant content of ferromagnetic material. Separation test by a magnet (inset of Fig. 14) confirmed that the composite catalyst could be easily separated.

3.8. Possible mechanisms

The highly efficient and magnetic heterogeneous Fenton-like catalyst was successfully fabricated by encapsulating Ni–Fe oxide nanoparticles into mesoporous SBA-15. Especially, when iron is incorporated on the surface of second (nickel) oxide, small size and well dispersed nanoparticles were obtained. This phenomenon can be explained by “seed effect” that the first impregnated metal oxide (host) acted as seeds for the growth of second metal oxide nanoparticles [17]. On the other side, strong metal-support interaction present between nickel species (host) and surface of SBA-15 was responsible for the spherical or ellipsoidal nanoparticles, and only large agglomerates of $\text{NiO}_y/\text{FeO}_x$ on SBA-15 surface (shown in Fig. S7 in Supporting information) were obtained due to the weak interaction between iron oxide and silica support if iron oxide(s) was used as host.

Furthermore, it has been stated previously that mixed-phase is very important to the catalytic activity of the catalyst because cooperatively enhanced performances can be achieved by the combination of respective properties of each phase [2,3,6,42]. In this study, it can be observed that mixed phases of nickel exist in the $\text{FeO}_x/\text{NiO}_y/\text{SBA-15}$, and the catalyst displayed perfect dye degradation and utilization efficiency of H_2O_2 . These phenomena can be easily explained by the standard redox potentials of nickel species. First of all, there is slight gap between $E_{\text{Ni(III)/Ni(II)}}^0$ (+1.74 V) and $E_{\text{H}_2\text{O}_2/\text{H}_2\text{O}}^0$ (+1.776 V), so the reaction $\text{Ni(II)} + \text{H}_2\text{O}_2 \rightarrow \text{Ni(III)} + \bullet\text{OH} + \text{OH}^-$ is progressed slowly. Second, Ni(0) cannot form a redox cycle and produce $\bullet\text{OH}$ because $E_{\text{Ni(II)/Ni}}^0$ is only -0.25 V, but the reduction of the Fe(III) to Fe(II) in Fenton-like reaction can be facilitated by the existence of Ni(0) in the catalyst, because the reaction $\text{Fe(III)} + \text{Ni(0)} \rightarrow \text{Fe(II)} + \text{Ni(II)}$ can easily occur. Finally, the nickel species are less reactive toward hydrogen peroxide than the iron species, so the lifetime of adsorbed H_2O_2 was prolonged [39], which facilitates H_2O_2 utilization and increases the TOC removal. Above all, the Fenton-like degradation occurs sequentially or/and simultaneously among the mixed oxides, which cooperated seamlessly at the nanometer level and the reactions can be described as follow:



Last but not the least, besides Fe_3O_4 , Ni(0) contributes part of magnetism to the $\text{FeO}_x/\text{NiO}_y/\text{SBA-15}$, which is very useful for the separation of the catalyst. In this study, part of Ni species were reduced to Ni(0) , while zero-valent Fe was not discovered. This is because bonds dissociation energies of Fe–O is 407 KJ/mol, while Ni–O is 366 KJ/mol, so the Ni–O in Ni_2O_3 was easier to crack and to form Ni(0) under same temperature.

4. Conclusions

In the present work, a uniform and highly dispersed nickel-iron catalyst was successfully fabricated and used in Fenton-like degradation. Such uniform size and homogeneous distribution were obtained by incorporating iron on the surface of a nickel (host) oxide. This catalyst displays excellent performances for dye AR 73 removal with high mineralization degree and utilization efficiency of H_2O_2 . Investigations of chemical components and catalytic tests showed that mixed phases including Ni(0) and NiO all have positive contribution to the high catalytic activity. All in all, owing to superior synergistic effects between Fe and Ni species in $\text{FeO}_x/\text{NiO}_y/\text{SBA-15}$, the catalyst displays a perfect potential in H_2O_2 favorite reactions.

Acknowledgements

The authors acknowledge financial support from 863 Research Project (2013AA065202), the National Natural Science Foundation of China (No. 21377111) and the Cultivation Fund of the Key Scientific and Technical Innovation Project, Ministry of Education of China (No. 708052). We also thank the staff at beamlines BL14W at the Shanghai Synchrotron Radiation Facility (SSRF) for providing the beam time and data analysis.

Appendix A. Supplementary data

Supplementary data associated with this article can be found, in the online version, at <http://dx.doi.org/10.1016/j.apcatb.2015.05.034>

References

- [1] Q. Fu, F. Yang, X. Bao, Acc. Chem. Res. 46 (2013) 1692–1701.
- [2] G. Chen, Y. Zhao, G. Fu, P.N. Duchesne, L. Gu, Y. Zheng, X. Weng, M. Chen, P. Zhang, C.W. Pao, Science 344 (2014) 495–499.
- [3] L. Xu, X. Li, J. Ma, Y. Wen, W. Liu, Appl. Catal. A: General 485 (2014) 91–98.
- [4] M. Cargnello, V.V. Doan-Nguyen, T.R. Gordon, R.E. Diaz, E.A. Stach, R.J. Gorte, P. Fornasiero, C.B. Murray, Science 341 (2013) 771–773.
- [5] J. Cai, H. Ma, J. Zhang, Q. Song, Z. Du, Y. Huang, J. Xu, Chem. A Eur. J. 19 (2013) 14215–14223.
- [6] X. Li, X. Liu, L. Xu, Y. Wen, J. Ma, Z. Wu, Appl. Catal. B: Environ. 165 (2015) 79–86.
- [7] S. Navalón, R. Martín, M. Alvaro, H. García, Angew. Chem. Int. Ed. 49 (2010) 8403–8407.
- [8] C. Rossy, J. Majimel, E. Fouquet, C. Delacote, M. Boujtita, C. Labrugere, M. Treguer Delapierre, F.X. Felpin, Chem. A Eur. J. 19 (2013) 14024–14029.
- [9] G. Yang, N. Tsubaki, J. Shamoto, Y. Yoneyama, Y. Zhang, J. Am. Chem. Soc. 132 (2010) 8129–8136.
- [10] C. Yu, J. He, Chem. Commun. 48 (2012) 4933–4940.
- [11] Z.M. Cui, Z. Chen, C.Y. Cao, L. Jiang, W.G. Song, Chem. Commun. 49 (2013) 2332–2334.
- [12] A. Ungureanu, B. Dragoi, A. Chiriac, C. Ciotonea, S. Royer, D. Duprez, A.S. Mamede, E. Dumitriu, ACS Appl. Mater. Interfaces 5 (2013) 3010–3025.
- [13] M.L. Rache, A.R. García, H.R. Zea, A.M. Silva, L.M. Madeira, J.H. Ramírez, Appl. Catal. B: Environ. 146 (2014) 192–200.
- [14] F. Duarte, F. Maldonado-Hódar, A. Pérez-Cadenas, L.M. Madeira, Appl. Catal. B: Environ. 85 (2009) 139–147.
- [15] S. Navalón, M. Alvaro, H. García, Appl. Catal. B: Environ. 99 (2010) 1–26.
- [16] M. Xia, M. Long, Y. Yang, C. Chen, W. Cai, B. Zhou, Appl. Catal. B: Environ. 110 (2011) 118–125.

- [17] H. Lim, J. Lee, S. Jin, J. Kim, J. Yoon, T. Hyeon, *Chem. Commun.* (2006) 463–465.
- [18] Y. Wang, H. Zhao, G. Zhao, *Appl. Catal. B: Environ.* 164 (2015) 396–406.
- [19] P. Shukla, S. Wang, H. Sun, H.-M. Ang, M. Tadé, *Chem. Eng. J.* 164 (2010) 255–260.
- [20] C.H. Liu, N.C. Lai, S.C. Liou, M.W. Chu, C.H. Chen, C.M. Yang, *Micropor. Mesopor. Mater.* 179 (2013) 40–47.
- [21] C. Cornu, J.L. Bonardet, S. Casale, A. Davidson, S. Abramson, G. André, F. Porcher, I. Grčić, V. Tomasic, D. Vujevic, N. Koprivanac, *J. Phys. Chem. C* 116 (2012) 3437–3448.
- [22] P.F. Wang, H.X. Jin, M. Chen, D.F. Jin, B. Hong, H.L. Ge, J. Gong, X.L. Peng, H. Yang, Z.Y. Liu, X.Q. Wang, *J. Nanomater.* 2012 (2012) 1–7.
- [23] A. Dhakshinamoorthy, S. Navalon, M. Alvaro, H. Garcia, *ChemSusChem* 5 (2012) 46–64.
- [24] M.Y. Cheng, C.J. Pan, B.J. Hwang, *J. Mater. Chem.* 19 (2009) 5193.
- [25] Z. Han, Y. Dong, S. Dong, *J. Hazard. Mater.* 189 (2011) 241–248.
- [26] S.H. Tian, Y.T. Tu, D.S. Chen, X. Chen, Y. Xiong, *Chem. Eng. J.* 169 (2011) 31–37.
- [27] Y.Z. Wen, C.S. Shen, Y.Y. Ni, S.P. Tong, F. Yu, *J. Hazard. Mater.* 201 (2012) 162–169.
- [28] C.S. Shen, Y.Z. Wen, Z.L. Shen, J. Wu, W.P. Liu, *J. Hazard. Mater.* 201 (2011) 209–215.
- [29] C. Shen, Y. Shen, Y. Wen, H. Wang, W. Liu, *Water Res.* 45 (2011) 5200–5210.
- [30] J. Shi, Z. Ai, L. Zhang, *Water Res.* 59 (2014) 145–153.
- [31] M. Luo, S. Yuan, M. Tong, P. Liao, W. Xie, X. Xu, *Water Res.* 48 (2014) 190–199.
- [32] A.H. Lu, J.J. Nitz, M. Comotti, C. Weidenthaler, K. Schlichte, C.W. Lehmann, O. Terasaki, F. Schuth, *J. Am. Chem. Soc.* 132 (2010) 14152–14162.
- [33] Z.J. Wang, Y.B. Xie, C.J. Liu, *J. Phys. Chem. C* 112 (2008) 19818–19824.
- [34] T. Brezesinski, M. Groenewolt, M. Antonietti, B. Smarsly, *Angew. Chem. Int. Ed.* 45 (2006) 781–784.
- [35] B. Tian, T. Wang, R. Dong, S. Bao, F. Yang, J. Zhang, *Appl. Catal. B: Environ.* 147 (2014) 22–28.
- [36] S.G. Christoskova, N. Danova, M. Georgieva, O. Argirov, D. Mehandzhiev, *Appl. Catal. A: General* 128 (1995) 219–229.
- [37] N.N. Tušar, D. Maučec, M. Rangus, I. Arčon, M. Mazaj, M. Cotman, A. Pintar, V. Kaučič, *Adv. Funct. Mater.* 22 (2012) 820–826.
- [38] W.F. de Souza, I.R. Guimarães, L.C. Oliveira, A.S. Giroto, M.C. Guerreiro, C.L. Silva, *Appl. Catal. A: General* 381 (2010) 36–41.
- [39] C. Lee, D.L. Sedlak, *Environ. Sci. Technol.* 42 (2008) 8528–8533.
- [40] W. Luo, L. Zhu, N. Wang, H. Tang, M. Cao, Y. She, *Environ. Sci. Technol.* 44 (2010) 1786–1791.
- [41] C. Lee, C.R. Keenan, D.L. Sedlak, *Environ. Sci. Technol.* 42 (2008) 4921–4926.
- [42] J.B. Park, J. Graciani, J. Evans, D. Stacchiola, S. Ma, P. Liu, A. Nambu, J.F. Sanz, J. Hrbek, J.A. Rodriguez, *Proc. Natl. Acad. Sci.* 106 (2009) 4975–4980.